Materials and Design 111 (2016) 382–388

Contents lists available at ScienceDirect

Materials and Design

journal homepage: www.elsevier.com/locate/matdes

Characterization and modeling of a MoTaVWZr high entropy alloy

M. Suarez Anzorena [a,b], A.A. Bertolo [a,b], L. Gagetti [a,b,c,d], A.J. Kreiner [a,b,c,d], H.O. Mosca [a,b,e], G. Bozzolo [f], M.F. del Grosso [a,d,e,*]

[a] Gerencia de Investigación y Aplicaciones, Comisión Nacional de Energía Atómica, Av. Gral. Paz 1499, B1650KNA San Martín, Buenos Aires, Argentina
[b] Instituto Sabato, Universidad Nacional de San Martín (UNSAM)- Comisión Nacional de Energía Atómica (CNEA), San Martín, Buenos Aires, Argentina
[c] Escuela de Ciencia y Tecnología, Universidad Nacional de San Martín (UNSAM), B1650HMQ San Martín, Buenos Aires, Argentina
[d] Consejo Nacional de Investigaciones Científicas y Técnológicas (CONICET), Rivadavia 1917, C1033AAJ Ciudad de Buenos Aires, Argentina
[e] GRUCAMM, UTN Gral. Pacheco, H. Yrigoyen 288, B1617FRP General Pacheco, Buenos Aires, Argentina
[f] Loyola University Maryland, 4501 N. Charles St, Baltimore, MD 21210, USA

HIGHLIGHTS

- MoTaVWZr alloy was prepared from an equimolar mixture.
- The alloy solidifies as two body-centered cubic (bcc) crystal phases, and two secondary phases (laves C15 and hcp).
- Crystal structure, density and Vickers microhardness are reported for this high entropy alloy.
- Atomistic modeling, using the BFS method, results are in agreement and support the experimental findings.

GRAPHICAL ABSTRACT

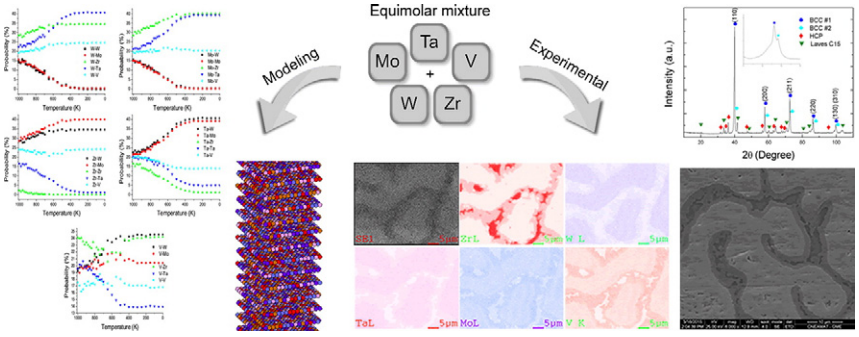

ARTICLE INFO

Article history:
Received 27 May 2016
Received in revised form 23 August 2016
Accepted 2 September 2016
Available online 4 September 2016

Keywords:
High-entropy alloys
Alloy design
Microstructure
Monte Carlo simulation

ABSTRACT

As part of a project for developing Accelerator–Based Boron Neutron Capture Therapy (AB-BNCT), for which the generation of neutrons through nuclear reactions like ^{9}Be(d,n) is necessary, a new material that preserves its physical and mechanical properties for a sufficient length of time under irradiation conditions and hydrogen damage is needed. In this work, a high entropy MoTaVWZr alloy (HEA) is considered for this task, because each one of the constituents is already good by itself under extreme irradiation condition. The structure, microstructure, density, Vickers hardness and melting temperature are reported for this HEA. Atomistic modeling results are in agreement with the experimental findings.

1. Introduction

In the last few years there has been an increasing need to develop new materials capable of resisting damage caused by particle irradiation. Among other examples, these are needed for fusion reactors first walls, neutron production targets for nuclear and medical use, for electronic applications, and the transportation industry [1,2].

Currently, a high power neutron production target is being designed at the Argentine Atomic Energy National Commission (CNEA). This is part of a project for developing Accelerator–Based Boron Neutron Capture Therapy (AB-BNCT) for which the generation of neutrons through nuclear reactions like ^{9}Be(d,n) is necessary [3,4]. To produce

* Corresponding author at: Gerencia de Investigación y Aplicaciones, CNEA, Av. Gral. Paz 1499, B1650KNA San Martín, Buenos Aires, Argentina.
E-mail address: delgrosso@tandar.cnea.gov.ar (M.F. del Grosso).

http://dx.doi.org/10.1016/j.matdes.2016.09.006
0264-1275/

the neutron beam, suitable for AB-BNCT, the Be target will be hit by a deuteron beam of 1.4 MeV with a current of about 30 mA. Under such conditions, the target has to be able to withstand the mechanical and thermal stresses produced by such an intense beam. In particular, the target should be able to dissipate an energy density of up to 1 kW/cm^2 and preserve its physical and mechanical properties, as well as its integrity (i.e., no blistering, melting, or cracking), for a sufficient length of time under irradiation and hydrogen damage conditions. To meet these requirements, the target is proposed to consist of a thin neutron producing material deposited on a thin layer of another material that stops the beam. The nature of the substrate material is an obvious concern. Astrelin et al. performed experiments to select radiation resistant materials for the target substrate and estimate the target lifetime. It was found that Ta and V support ion beam irradiation longer than others [5]. Mo and W were also studied by several authors who found that these materials present small blisters and support fluences higher than other metals, of about 1×10^{22}–1×10^{23} ions/m^2 [6–10].

The search for materials that can withstand radiation damage for extended periods of time is constrained by a limited range of options (restricted to pure metal sheets of W, Mo, Ta, V and, with less success, Fe and steels). However, the growing field of high entropy alloys (HEAs) opens new possibilities. These alloys constitute an exciting new class of materials, which have shown great promise for applications under extreme conditions [11–14]. HEAs are composed of five or more elements, typically of similar size and mixed in a near equimolar ratio. These alloys, due to the large number of elements, have high configurational entropy, and they tend to form substitutionally disordered solid solutions with simple crystal structures, such as face-centered (fcc), body-centered cubic (bcc) [15] or even hexagonal close packed (hcp) [16]. The term HEA, which is customarily used to describe single phase multicomponent alloys, is hereby used in the same context as done in other similar studies [1,17,18] where even the presence of minor secondary phases does not preclude the system from being considered by its main characteristic, which is a predominant solid solution. HEAs have attracted significant attention due to their potential beneficial mechanical, magnetic, and electrochemical characteristics, such as high strength, high thermal stability and oxidation resistance [11–19].

More importantly, there are indications that HEAs are resistant to radiation damage [20–24]. While conventional materials develop a large number of crystal defects in a radiation environment, HEAs may transform locally into a glass as a result of extensive radiation damage and then recrystallize into a disordered solid solution, as if they underwent a self-healing process [25].

The possibilities for nuclear applications are intriguing and highly promising, due to their resistance to radiation, lack of bubbles, and their ability to avoid collecting interstitial H. Therefore, the purpose of this work is to gain knowledge of HEAs for potential future applications as a backing material in a neutron production target. With this use in mind, a new HEA of five components (Mo, Ta, V, W, and Zr) at equimolar ratio is hereby proposed. Mo, Ta, V, and W were selected because they are radiation resistant materials and Zr because it is a getter material that has the ability to collect free gases, such as H, at low temperature. The MoTaVWZr alloy developed in this work was characterized and the results were compared to those predicted by a recently proposed atomistic method particularly designed for HEAs [26]. To our knowledge, no previous research has been done on this particular HEA.

2. Materials and methods

2.1. Experimental

The MoTaVWZr alloy was prepared from an equimolar mixture of the corresponding elements by arc melting in a high purity Argon atmosphere. Under this condition the sample was re-melted, flipped for each melt to improve homogeneity, and then cut off in four pieces for a new melt. The alloy was re-melted and flipped twelve times, and was in a liquid state for about one minute during each melting event. In order to characterize the obtained alloy, the samples were cut using a diamond cut-off wheel to expose a flat surface of the cross section. Then, the exposed surface was ground by #220, #320, #400, #600 abrasive papers, before being polished with 6 μm and 1 μm steel cloth. This process was analyzed using an Olympus BX60M optical microscope.

The sample was annealed at 1100 °C for 24 and 72 h and characterized in the as-cast form and after the annealing, as it is essential to make experimental observations on a material where effort was made to reducing casting defects.

The crystal structure was characterized by an X-Ray diffractometer (Panalitycal Empyrean, XRD, with Cu radiation target) with the 2θ scan ranging from 10° to 110°. SEM micrographs were taken with a Philips ESEM QUANTA 200. Qualitative and quantitative analysis of the composition was performed by energy dispersive spectroscopy (EDS) mapping.

The alloy density was measured with a precision analytical balance Mettler H54 by means of the hydrostatic method, under a liquid cyclohexane bath settled at 20 °C. Dry and wet measurements were determined with an accuracy of 0.001 g. Vickers microhardness was measured on polished cross-section surfaces using a Leitz Wetzlar Durimet instrument.

2.2. Theory: the BFS method for alloys

A simple analytical procedure [26] was recently developed for the study of HEAs by means of large atomistic simulations that use the Bozzolo-Ferrante-Smith (BFS) method for the energetics [27]. The algorithm determines, for a given alloy concentration, the atomic coordination between atoms of different species, and how they evolve with temperature during the simulated annealing process [26]. As a result, the algorithm predicts the necessary conditions (temperature and concentration) that result in a final disordered solution, the main feature of HEAs. The interaction between atoms is determined via the BFS method, a quantum approximate method based on the assumption that the energy of formation of a given atomic configuration can be defined as the sum of the individual atomic contributions, $\Delta H = \sum_i \varepsilon_i$. Each contribution, ε_i, consists of a strain energy term, ε_i^S, which accounts for the change in geometry relative to a single monatomic crystal of the reference atom i, and a chemical energy term, ε_i^C, where every neighbor of the atom i is in an equilibrium lattice site of a crystal of species i, but retaining its chemical identity. A reference chemical energy, $\varepsilon_i^{C_0}$, is also included to completely separate structural and chemical features. A coupling function, g_i, ensures the correct volume dependence of the BFS chemical energy contribution. The contribution of atom i to the energy of formation of the system is then given by

$$\varepsilon_i = \varepsilon_i^S + g_i\left(\varepsilon_i^C - \varepsilon_i^{C_0}\right) \quad (1)$$

First-principles calculations using the Linearized Augmented Plane Wave method [28] were used to determine single-element and interaction parameters for W, Ta, Mo, V, and Zr. The single element parameters were obtained from the zero temperature equation of state of the pure bcc solids, while the interaction parameters were obtained from the energy of formation curves (as a function of volume) for the bcc-based binary combinations of all the elements.

The temperature evolution was obtained from large scale Monte Carlo-Metropolis simulations [29]. For brevity, we direct the reader to previous studies [30–34] for the necessary details of the BFS method [27], the parameterization needed to perform the simulations, and operational equations as well as previous BFS applications to multicomponent systems [29–31,34,35].

It should be noted that all simulations were performed in cells with a uniform lattice parameter, optimized at every temperature step. This restriction, however, is irrelevant if the system evolves into a solid

solution and, to a lesser extent, if there are secondary phases, which can only be perceived as limited domains in the computational cell with different composition than the matrix.

It is worth noting that a direct comparison of BFS predictions of equilibrium alloy properties against ab initio results, and the handling and influence of the parameterization on the accuracy with which the method reproduces the process of alloy formation has been documented in a previous study [36]. It was found that the method provides highly accurate results, in comparison to first-principles, near or at equilibrium. In addition, this work established a range of validity for the method in reference to first-principles results, also introducing a simple algorithm for the determination of equilibrium properties of ordered alloy systems, illustrated with applications to binary and higher order systems, thus maximizing the flow of information carried in the first-principles-based parameters.

3. Results and discussion

3.1. Experimental results

3.1.1. Crystal structure

The X-ray diffraction patterns of the as-cast and annealed MoTaVWZr alloy are shown in Fig. 1(a). The first five major diffraction peaks in the X-ray patterns have been identified to belong to two body-centered cubic (bcc) phases. The indices of the crystal planes corresponding to the X-ray diffraction peaks (●) are shown in the Fig. 1(b). The lattice parameters of the two bcc phases were determined to be $a_1 = 3.19$ Å and $a_2 = 3.18$ Å, both in as-solidified and after the annealing. Additional low-intensity diffraction peaks in the X-ray pattern indicated the presence of minor secondary phases. The peaks identified with (♦) match up with the hexagonal close-packed (hcp) phase of Zr, and the additional minor peaks (▼) correspond to a C15 Laves phase. These secondary phases are seen in the as-cast and annealed samples. These results indicate that the crystal structure formed in the alloy during solidification is stable upon heating at least up to 1100 °C. In all cases, the samples annealed for 24 and 72 h. were analyzed, with no relevant differences between them. In what follows, any mention to experimental results will refer to the 72 h. case, unless specifically mentioned that there is a difference with respect to the 24 h. sample.

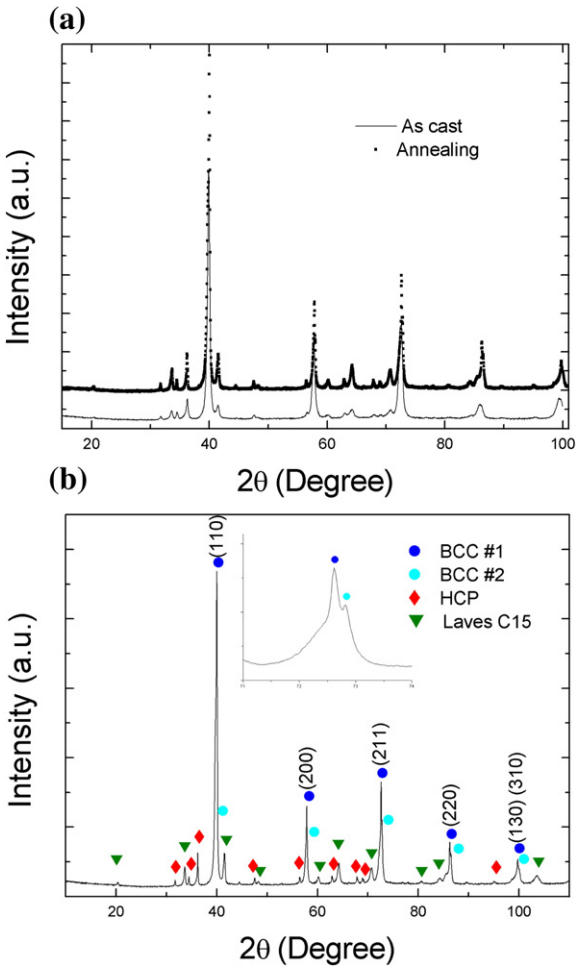

Fig. 1. X-ray diffraction pattern of the MoTaVWZr alloy: (a) In as-cast and after the annealing. (b) In the annealed alloy the peaks are well defined and the indexed peaks belong to two BCC, a Laves C15, and a HCP crystal phases.

3.1.2. Density and hardness

The density of the alloy was experimentally determined to be $\rho_{exp} = 11.400 \pm 0.001$ g/cm^3 by the hydrostatic method. The Vickers microhardness (H_v) of the alloy was measured in five selected locations under a 1000 g load applied for 15 s. The value was 6690 ± 60 MPa. Density and Vickers microhardness values reported in previous works [11,13] are shown in Table 1 for each one of the alloy constituent metals. The MoTaVWZr alloy density and microhardness experimental values are also indicated. As it can be seen in Table 1, the measured Vickers microhardness for this alloy (6690 MPa) considerably exceeds the corresponding value for pure W (3430 MPa), however, the sample density (11.400 g/cm^3) is lower than the density of pure W (19.30 g/cm^3). The exceptional microhardness of this alloy is greater than that of any individual constituent, this behavior is mainly attributed to the local lattice distortion and solid-solution strengthening effects [13,37,38].

3.1.3. Microstructure

A polished cross-section of equimolar MoTaVWZr alloy is shown in Fig. 2. Normal mode SEM micrographs were taken with different magnifications to evaluate in detail the microstructure and properties of the as-cast (a, b and c) and annealed alloy (d).

The as-cast button reveals a non-uniform grain size distribution, with a thin dendritic structure in the external part of the sample (Fig. 2(a)), and larger grains in the inner regions varying in size from 20 μm to 100 μm (Fig. 2(b)). The constitutional undercooling leads to the formation of dendritic structures; in dendritic growth, the mass of the low melting temperature solute is ejected between the dendrite arms and causes micro-segregation.

In Fig. 2(c) and (d), the interdendritic microstructure is clearly seen in both the as-cast and annealed alloy, respectively. The micrographs show grains with round boundaries (light zone) and an interdendritic region (dark background zone). In the as-cast sample some spherical intergranular precipitates over the interdendritic zone are observed. After the annealing, those precipitates form a continuous phase around the grain boundary. Lastly, fine intergranular precipitates are embedded in the interdendritic zone.

EDS compositional analyses of the as-cast alloy and after annealing for 24 and 72 h., were performed. The atomic percentage of each element measured in all the zones: G (grain zone), IG (intergranular zone) and FIG (fine intergranular zone), are listed in Table 2. It is interesting to note that the microstructure of this alloy was still present after heating at 1100 °C for 24 and 72 h. This result supports previous

Table 1
Density (ρ), Vickers microhardness (H_v) and melting temperature (T_m) of the pure metals [11,13] and experimental values for the MoTaVWZr alloy (this work).

	Mo	Ta	V	W	Zr	MoTaVWZr
ρ (g/cm^3)	10.28	16.65	6.11	19.25	6.51	11.4
H_v (MPa)	1530	873	628	3430	903	6690
T_m (K)	2896	3290	2183	3695	2128	–

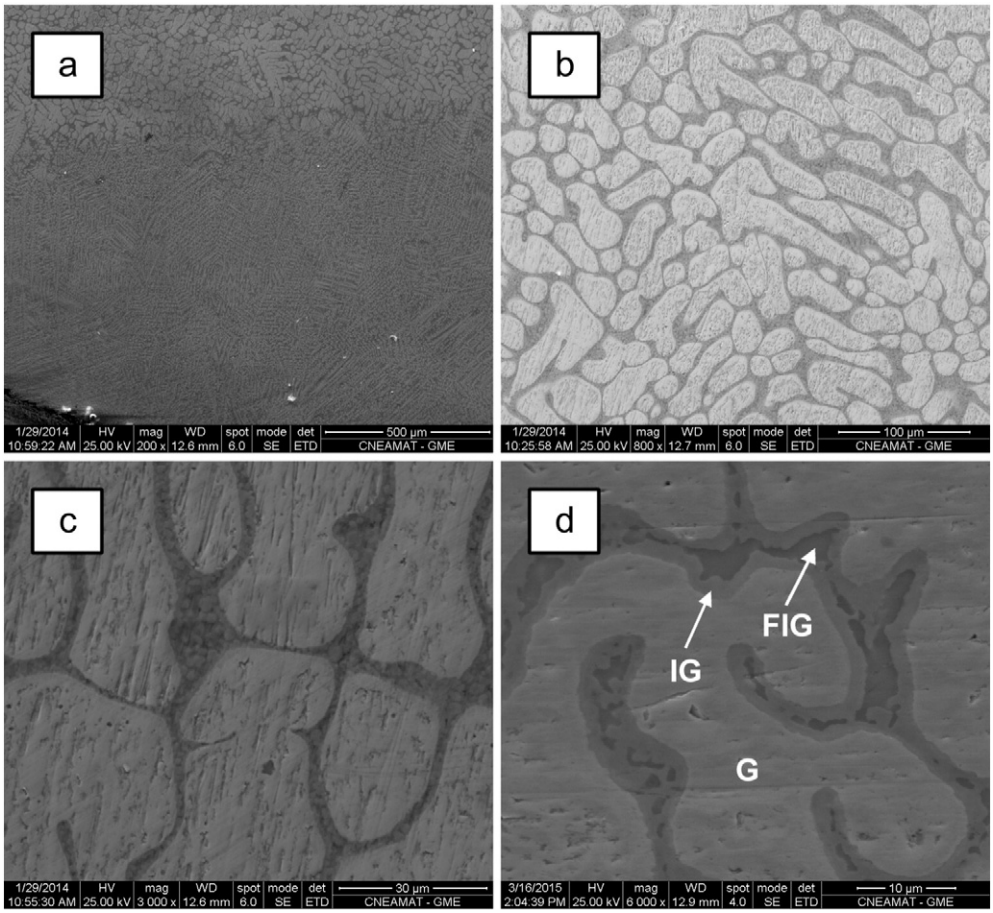

Fig. 2. SEM micrographs of a polished cross section of the (a–c) as-cast and (d) annealed MoTaVWZr alloy, indicating the grains (G), the intergranular regions (IG), and the fine intergranular zone (FIG).

observations of strongly reduced diffusivity of elements in high entropy alloys [12]. The measurements show that the intergranular region is rich in Zr in the as-cast sample, followed by V and Mo, but after annealing at 1100 °C this region has the elements more evenly distributed. This is not the case in the grain zone, where the composition remained stable after the annealing.

The mapping performed with EDS in the annealed alloy (Fig. 3) gives a relative intensity of the distribution of the five elements and a qualitative picture for the segregation characteristics of each constituent. The high pixel density area in Fig. 3 indicates an elevated concentration of a given element, while low density areas (nearly white) indicate lack of such element. The pictures show that the distribution of these elements is non-homogeneous. The grains are enriched with heavier elements (W and Ta), while the intergranular region (IG) shows the five elements homogeneously distributed around the grains (G) and discrete areas very rich in Zr (FIG), marked in Fig. 2(d). Presumably, the asymmetry in melting temperature between constituents leads W to solidify first in the dendritic microestructure, and Zr to segregate from it to the interdendritic regions.

Summarizing, the as-cast and the annealed samples exhibit a similar microstructure. The observations suggest that the alloy could probably be described as a multielement bcc grain zone (G), an intergranular zone (IG) corresponding to a very similar bcc structure (in spacing and composition, as seen in the X-ray patterns), with embedded Zr-rich Laves phases, and a fine intergranular zone (FIG) with Zr-rich hcp-based precipitates. Further TEM analysis would be necessary to ascertain this interpretation of the microstructure of this alloy. Recent results support the possibility that this interpretation is correct, as the studies report a Zr-rich inter-grain phase [39,40].

3.2. Simulation results

The BFS-based algorithm [26] is mainly designed to study the transition into the high entropy regime, in terms of composition, helping to determine the necessary concentrations of each element and the temperature at which such transition takes place. It is at its most useful when the number of elements is large and there is a need to evaluate whether the inclusion of a given element, in specific amounts, facilitates the formation of a homogeneous solid solution. In this case, the predetermined fixed composition of the experimental alloy makes such analysis unnecessary, but it is still useful to determine the bulk properties of the alloy and confirm the experimental findings as well as confirming some details of the microstructure. The computational

Table 2
Chemical composition (at.%) of the bulk, the grains (denoted as "G"), the intergranular regions (denoted as "IG"), and the fine intergranular zone (denoted as "FIG") in the MoTaVWZr alloy.

	Regions	Mo	Ta	V	W	Zr
As-cast	G	21.90	28.93	16.05	31.39	1.73
	IG	20.97	6.64	28.82	2.48	41.09
	FIG	–	3.94	4.74	1.90	89.41
Annealed 1100 °C 24 h	G	25.13	27.10	12.66	31.86	3.25
	IG	20.13	17.08	18.88	15.60	28.30
	FIG	3.45	3.03	5.50	1.29	86.72
Annealed 1100 °C 72 h	G	26.98	26.80	12.73	29.75	3.73
	IG	21.22	18.02	17.66	18.81	24.29
	FIG	–	3.73	8.79	1.59	85.88

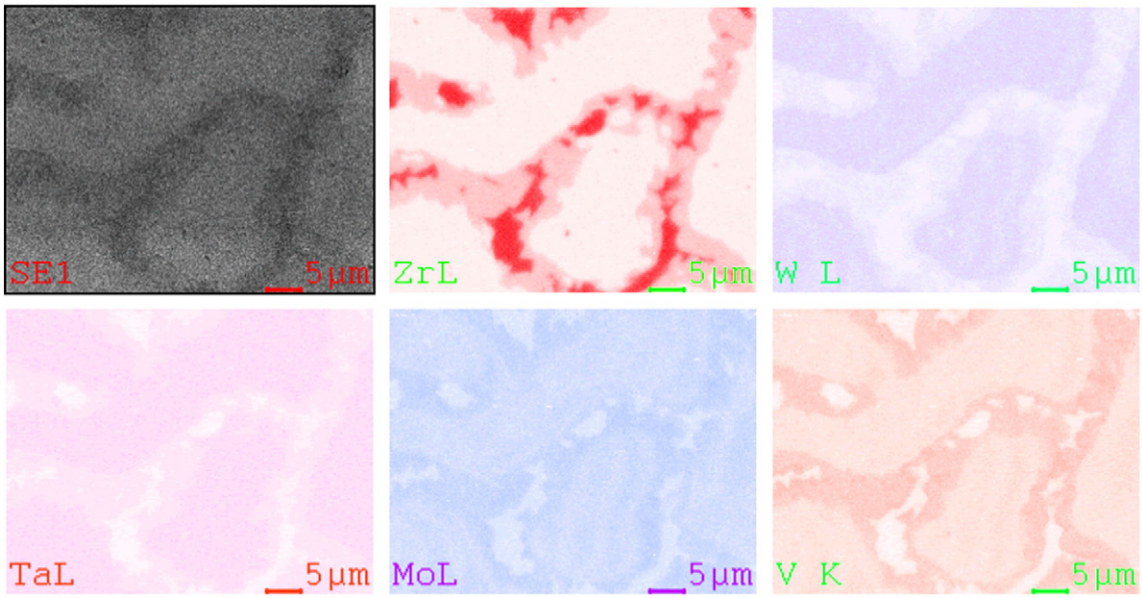

Fig. 3. Energy Dispersive Spectroscopy (EDS) map of the cross section of the MoTaVWZr alloy. The relative intensity of each element map gives a qualitative sense for the segregation characteristics of that constituent.

cell is periodic in all three directions describing a bcc lattice (a cube with 15 × 15 × 26 atoms). The temperature cycle starts at an artificially high temperature, beyond the highest melting point of the pure elements, in order to ensure maximum disorder, and continues with steadily decreasing temperatures down to 0 K. At each temperature step, the cell is allowed to uniformly breathe to optimize its lattice parameter. It should be noted, however, that throughout the simulation the symmetry of the cell remains unchanged (a software limitation, not a property of the system). Keeping in mind that the goal of the simulation is to identify the general features of the distribution of the different atomic species, the effect of this restriction would be limited. The density was obtained by computing the corresponding volume, while the value of the mass was obtained by properly including the atomic weight and concentration of each element. The values for the lattice parameter and density (calculated at 300 K) for the resulting bcc solid solution are in good agreement with experimental measurements, as shown in Table 3. The computed value for the melting temperature, determined from the equation of state at zero temperature [30] is also reported, as the experimental value is not known.

Within the constraints imposed on the calculations (i.e. the use of a fixed-symmetry computational cell) the results for the computational cell for T > 1500 K show no signs of short-range order, thus supporting the notion that the combination of these elements would lead to a solid solution, if it is accepted that the underlying lattice indeed has a bcc structure. Forced to coexist in a single bcc lattice (uniform lattice parameter), the distribution of the different atoms could shed some light on the possibility that they would tend to form different domains, with slight differences in the concentrations of each one of the constituents. If no such differences are detected, it would suggest that such alloy would consist of a single bcc structure. If they are detected, it could be taken as an indication that more than one bcc-based structure, very similar in spacing and composition, may be found.

Table 3
Comparison between experimental and simulation values of the lattice parameter (a), density (ρ) and melting temperature (T_m). The simulation values were computed at 300 K.

	a (Å)	ρ (g/cm^3)	T_m (K)
Experimental (BCC1/2)	3.19/3.18	11.4	–
Simulation	3.24	11.74	2600

The simulation results are best described in terms of the short-range order coordination matrices, ρ_{XY} (for first nearest-neighbors, FNN) and μ_{XY} (for second nearest-neighbors, SNN), which give the probability that a given atom of species X may have an atom Y as a FNN or as a SNN, respectively. The evolution with temperature for each matrix element is shown in Fig. 4(a) (for FNN) and Fig. 4(b) (for SNN). The plot shows results between 1500 and 0 K (as opposed to higher temperatures) as there are no qualitative differences regarding the behavior of the probabilities above 1500 K.

Unlike previous applications of this algorithm to other multicomponent systems [26,29,30], this case is straightforward: the evolution of all matrix elements as a function of descending temperature shows a slow transition with descending temperature from a high temperature solid solution to a highly disordered pseudo-B2 structure, where the population of each sublattice is markedly different: one rich in W, and the other rich in Zr, as shown in Fig. 4. The solid solution is represented by the fact that all probabilities tend to converge for T > 1500 K, indicating no particular preference for specific X—Y bonds. As the temperature decreases (1500 > T > 400 K), the matrix elements transition to a different regime, which is characterized by a subtle redistribution of the different elements in alternating sublattices, but it is not necessarily (as evidenced by the SNN correlation matrices) an indication of regular ordering.

For T > 1500 K, the nearly similar probabilities for all X—Y bonds suggest that a solid solution is the dominant feature of this system. The low temperature regime (T < 400 K) of the FNN and SNN coordination matrix elements may be succinctly described as follows: 1) In the case of V, the relatively constant diagonal elements ρ_{VV} and μ_{VV} indicate that V is rather equally distributed in all regions of the computational cell, with no preference for a particular sublattice (otherwise, the SNN matrix elements would be much larger). 2) Unlike V, the other elements show a trend towards partitioning to different sublattices, W and Mo in one, Ta and Zr in the other, as indicated by the vanishing FNN matrix elements and the correspondingly increasing SNN values, but the trend is not strong enough to suggest regular order. 3) Ta shows high correlation with Mo and W, and Mo shows high correlation with Zr, as indicated by the high values of the FNN matrix elements for these pairs, corroborated by the fact that the SNN values tends to zero as the temperature decreases, indicating that they are present both in the Mo-Ta-W and Mo-Ta-Zr regions of the alloy. 4) There are regions of high concentration of Zr, as indicated by ρ_{ZrZr} and the corresponding SNN matrix elements.

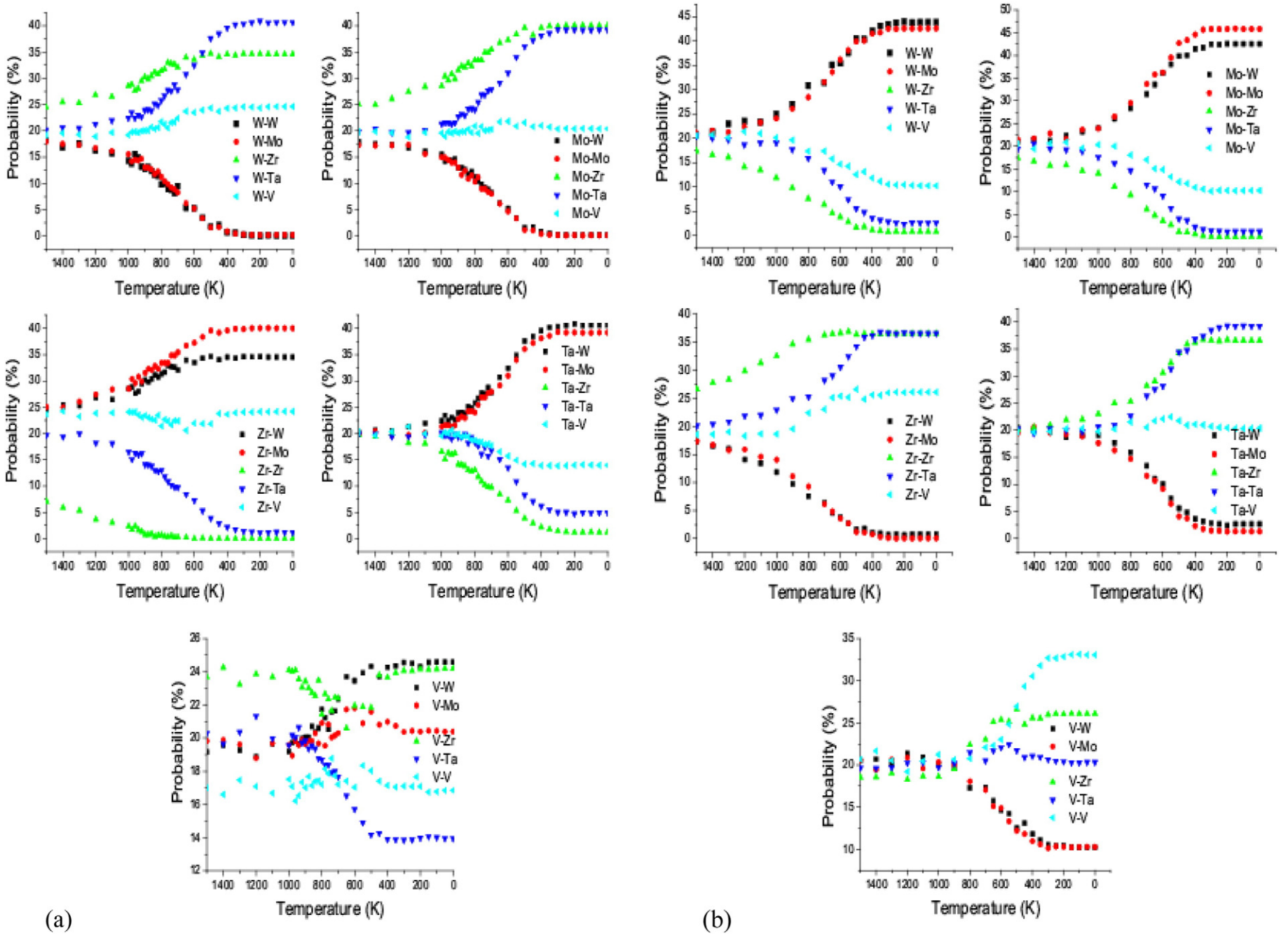

Fig. 4. (a). The evolution with temperature of the FNN coordination matrix ρ_{XY} for each element X. (b). The evolution with temperature of the SNN coordination matrix μ_{XY} for each element X.

Detection of a Zr-rich domain, within the context this simulation, just indicates a trend towards separation of some Zr from the solid solution. The constraints of the simulation preclude from determining whether this indicates Zr precipitation or just an artifice of the simulation.

As mentioned above, the restrictions imposed in the calculations preclude a direct comparison with the experimental results (Fig. 3 and Table 2). However, when the features identified in the computational cell are compared to the analysis of the annealed sample (where diffusion allows for a better homogenization of the intergranular region), they supplement the experimental description with some insight on the behavior at the atomic level.

4. Conclusions

For the purpose of developing a new material for a power neutron production target, a HEA of five components (Mo, Ta, V, W, and Zr) at equimolar ratio was examined. Mo, Ta, V, and W were selected because they are radiation resistant materials and Zr because it is a getter material that has the ability to collect free gases, such as H, at low temperature.

The MoTaVWZr alloy developed in this work was characterized by XRD, SEM and EDS. The density and Vickers microhardness were also measured. It was determined that the alloy has a predominant crystal structure identified as two body-centered cubic (bcc) crystal phases, and two secondary phases (laves C15 and hcp). The experimental density and hardness were determined to be 11.400 g/cm^3 and 6690 MPa, respectively.

An analytical procedure for the study of HEAs by means of large atomistic simulations that use the Bozzolo-Ferrante-Smith (BFS) method for the energetics, was implemented in order to supplement the experimental results. The computed values of the lattice parameter and density for the resulting bcc solid solution are in good agreement with experimental measurements.

As implemented in this work, limited to a computational cell with fixed symmetry, the theoretical support to the experimental work provided by the simulations does not constitute proof that such effort, in itself, can be considered a comprehensive design tool. However, it is possible, and worth considering in future work, that full and unrestricted implementation of the modeling approach could eventually facilitate the otherwise complex task of helping in the design of materials dealing with a large number of elements, as it is the case with most HEAs.

Based on the characteristics of these materials for their potential for radiation resistance, the next step will be the irradiation of the HEA as well as of the pure constituent materials in order to evaluate and compare the blistering threshold, under a proton beam.

Acknowledgements

Fruitful discussions with N. Bozzolo are gratefully acknowledged.

References

[1] Y. Zhang, T.T. Zuo, Z. Tang, M.C. Gao, K.A. Dahmen, P.K. Liaw, Z.P. Lu, Microstructures and properties of high-entropy alloys, Prog. Mater. Sci. 61 (2014) 1–93.
[2] M.C. Gao, J. Yeh, P.K. Liau, Y. Zhang, High-Entropy Alloys: Fundamentals and Applications, Springer, 2016.
[3] M.E. Capoulat, D.M. Minsky, A.J. Kreiner, Applicability of the ^{9}Be(d,n)^{10}B reaction to AB-BNCT skin and deep tumor treatment, Appl. Radiat. Isot. 69 (2011) 1684–1687.
[4] M.E. Capoulat, D.M. Minsky, A.J. Kreiner, Computational assessment of deep-sited tumor treatment capability of the ^{9}Be(d,n)^{10}B reaction for accelerator-based Boron Neutron Capture Therapy (AB-BNCT), Physica Medica: Eur. J. Med. Phys. 30 (2013) 133–146.
[5] V.T. Astrelin, A.V. Burdakov, P.V. Bykov, I.A. Ivanov, A.A. Ivanov, Y. Jongen, S.G. Konstantinov, A.M. Kudryavtsev, K.N. Kuklin, K.I. Mekler, S.V. Polosatkin, V.V. Postupaev, A.F. Rovenskikh, S.L. Sinitskiy, E.R. Zubairov, Blistering of the selected materials irradiated by intense 200 keV proton beam, J. Nucl. Mater. 396 (2010) 43–48.
[6] V.M. Sharapov, V.D. Alimvo, Deuterium acumulation in deposited tungsten films, Plasma Dev. Oper. 12 (2004) 299–303.
[7] M. Fukumoto, Y. Ohtsuka, Y. Ueda, M. Taniguchi, M. Kashiwagi, T. Inoue, K. Sakamoto, Blister formation on tungsten damaged by high energy particle irradiation, J. Nucl. Mater. 375 (2008) 224–228.
[8] M. Fukumoto, H. Kashiwagi, Y. Ohtsuka, Y. Ueda, Y. Nobuta, J. Yagyu, T. Arai, M. Taniguchi, T. Inoue, K. Sakamoto, Hydrogen behavior in damaged tungsten by high-energy ion irradiation, J. Nucl. Mat. 386-388 (2009) 768–771.
[9] R.A. Causey, T.J. Venhaus, The use of tungsten in fusion reactors: a review of the hydrogen retention and migration properties, Phys. Scr. T94 (2001) 9–15.
[10] A.A. Haasz, M. Poon, J.W. Davis, The effect of ion damage on deuterium trapping in tungsten, J. Nucl. Mater. 266–269 (1999) 520–525.
[11] O.N. Senkov, C.F. Woodward, Microstructure and properties of a refractory $NbCrMo_{0.5}$ $Ta_{0.5}TiZr$ alloy, Mater. Sci. Eng. A 529 (2011) 311–320.
[12] O.N. Senkov, G.B. Wilks, J.M. Scott, D.B. Miracle, Mechanical properties of $Nb_{25}Mo_{25}Ta_{25}W_{25}$ and $V_{20}Nb_{20}Mo_{20}Ta_{20}W_{20}$ refractory high entropy alloys, Intermetallics 19 (2011) 698–706.
[13] O.N. Senkov, G.B. Wilks, D.B. Miracle, C.P. Chuang, P.K. Liaw, Refractory high-entropy alloys, Intermetallics 18 (2010) 1758–1765.
[14] Y. Zhang, Y. Liu, Y. Li, X. Chen, H. Zhang, Microstructure and mechanical properties of a refractory $HfNbTiVSi_{0.5}$ high-entropy alloy composite, Mater. Lett. 174 (2016) 82–85.
[15] F. Zhang, C. Zhang, S.L. Chen, J. Zhu, W.S. Cao, U.R. Kattner, An understanding of high entropy alloys from phase diagram calculations, Calphad 45 (2014) 1–10.
[16] Y.J. Zhao, J.W. Qiao, S.G. Ma, M.C. Gao, H.J. Yang, M.W. Chen, Y. Zhang, A hexagonal close-packed high-entropy alloy: The effect of entropy, Mater. Des. 96 (2016) 10–15.
[17] B.S. Murty, J. Yeh, S. Ranganathan, High-entropy Alloys, Butterworth-Heinemann, 2014.
[18] S. Singh, N. Wanderka, B.S. Murty, U. Glatzel, J. Banhart, Decomposition in multicomponent AlCoCrCuFeNi high-entropy alloy, Acta Mater. 59 (2011) 182–190.
[19] B. Zhang, M.C. Gao, Y. Zhang, S.M. Guo, Senary refractory high-entropy alloy $Cr_xMoNbTaVW$, Calphad 51 (2015) 193–201.
[20] N.A.P. Kiran Kumar, K.J. Leonard, H. Bei, T.S. Byun, Y. Zhang, S.J. Zinkle, Ion irradiation effects on high entropy alloy, Fusion Reactor Materials Program 54 (2013) 145–153.
[21] T. Nagase, S. Anada, P.D. Rack, J.H. Noh, H. Yasuda, H. Mori, T. Egami, MeV electron-irradiation-induced structural change in the bcc phase of Zr-Hf-Nb alloy with an approximately equiatomic ratio, Intermetallics 38 (2013) 70–79.
[22] N.A.P. Kiran Kumar, K.J. Leonard, H. Bei, S.J. Zinkle, Microstructural stability and mechanical behavior of FeNiMnCr high entropy alloy under ion irradiation, Acta Mater. 113 (2016) 230–244.
[23] A.D. Pogrebnjak, I.V. Yakushchenko, O.V. Bondar, V.M. Beresnev, K. Oyoshi, O.M. Ivasishin, H. Amekura, Y. Takeda, M. Opielak, C. Kozak, Irradiation resistance, microstructure and mechanical properties of nanostructured (TiZrHfVNbTa)N coatings, J. Alloys Compd. 679 (2016) 155–165.
[24] S. Xia, Z. Wang, T. Yang, Y. Zhang, Irradiation behavior in high entropy alloys, J. Iron Steel Res. 22 (2015) 879–884.
[25] P.K. Liaw, T. Egami, Y. Zhang, F. Zhang, Radiation Behavior of High-Entropy Alloys for Advanced Reactors NEUP, 2015.
[26] M.F. del Grosso, G. Bozzolo, H.O. Mosca, Determination of the transition to the high entropy regime for alloys of refractory elements, J. Alloys Compd. 534 (2012) 25–31.
[27] J. Smith, T. Perry, A. Banerjea, J. Ferrante, G. Bozzolo, Equivalent-crystal theory of metal and semiconductor surfaces and defects, Phys. Rev. B 44 (1991) 6444–6465.
[28] P. Blaha, K. Schwarz, G.K.H. Madsen, D. Kvasnicka, J. Luitz, WIEN2K, An Augmented Plane Wave + Local Orbitals Program for Calculating Crystal Properties, Karlheinz Schwarz, Techn. Universität Wien, Austria, 2001.
[29] H.O. Mosca, G. Bozzolo, M.F. del Grosso, Thermal and physical properties of Al-Ni-Ru-M alloys, Mater. Sci. Eng. B 162 (2009) 99–105.
[30] M.F. del Grosso, H.O. Mosca, G. Bozzolo, Thermal and physical properties of B2 Al-Ir-X (X = Ni, Ru, Pd, Co, Fe) alloys, Intermetallics 18 (2010) 945–953.
[31] G. Bozzolo, J. Khalil, R.D. Noebe, Modeling of the site preference in ternary B2-ordered Ni-Al-Fe alloys, Comput. Mater. Sci. 24 (2002) 457–480.
[32] G. Bozzolo, J. Ferrante, J.R. Smith, Method for calculating alloy energetics, Phys. Rev. B 45 (1992) 493–496.
[33] G. Bozzolo, J.E. Garcés, Chapter 2 – atomistic modelling of surface alloys, The Chemical Physics of Solid Surfaces, Elsevier 2002, pp. 30–85.
[34] A. Wilson, G. Bozzolo, R.D. Noebe, J. Howe, Experimental verification of the theoretical prediction of the phase structure of a Ni-Al-Ti-Cr-Cu alloy, Acta Mater. 50 (2002) 2787–2800.
[35] G. Bozzolo, H.O. Mosca, A.M. Yacout, G. Hofman, Lanthanides migration in U-Zr based nuclear fuels, J. Nucl. Mater. 407 (2010) 228–231.
[36] J.E. Garces, G. Bozzolo, Determination of structural alloy equilibrium properties from quantum approximate methods, Phys. Rev. B 71 (2005) 134201.
[37] Y. Zou, S. Maiti, W. Steurer, R. Spolenak, Size-dependent plasticity in an $Nb_{25}Mo_{25}Ta_{25}W_{25}$ refractory high-entropy alloy, Acta Mater. 65 (2014) 85–97.
[38] S. Maiti, W. Steurer, Structural-disorder and its effect on mechanical properties in single-phase TaNbHfZr high-entropy alloy, Acta Mater. 106 (2016) 87–97.
[39] M. Heidelmann, M. Feuerbacher, D. Ma, B. Grabowski, Structural anomaly in the high-entropy alloy ZrNbTiTaHf, Intermetallics 68 (2016) 11–15.
[40] M.C. Gao, B. Zhang, S. Yang, S.M. Guo, Senary refractory high-entropy alloy HfNbTaTiVZr, Metal. Mater. Trans. A 47 (2015) 3333–3345.